Oxygen vacancy formation characteristics in the bulk and across different surface terminations of $La_{(1-x)}Sr_xFe_{(1-y)}Co_yO_{(3-\delta)}$ perovskite oxides for CO_2 conversion

Debtanu Maiti[1], Yolanda A. Daza[1], Matthew M. Yung[2], John N. Kuhn[1] and Venkat R. Bhethanabotla[1,*]

1. University of South Florida. Tampa, FL 33620

2. National Renewable Energy Laboratory. Golden, CO 80401

Keywords: perovskite oxides, oxygen vacancy, surface termination, CO_2 conversion

Abstract:

Density functional theory (DFT) based investigation of two parameters of prime interest – oxygen vacancy and surface terminations along (100) and (110) planes - has been conducted for $La_{(1-x)}Sr_xFe_{(1-y)}Co_yO_{(3-\delta)}$ perovskite oxides in view of their application towards thermochemical carbon dioxide conversion reactions. The bulk oxygen vacancy formation energies for these mixed perovskite oxides are found to increase with increasing lanthanum and iron content in the 'A' site and 'B' site, respectively. Surface terminations along (100) and (110) crystal planes are studied to probe their stability and their capabilities to accommodate surface oxygen vacancies. Amongst the various terminations, oxygen-rich (110) surface and strontium-rich (100) surfaces are the most stable, while transition metal-rich terminations along (100) revealed preference towards producing oxygen vacancies. The carbon dioxide adsorption strength, a key descriptor for CO_2 conversion reactions, is found to increase on oxygen vacant surfaces thus establishing the importance of oxygen vacancies in CO_2 conversion reactions. Amongst all the surface terminations, lanthanum-oxygen terminated surface exhibited the strongest CO_2 adsorption strengths. The theoretical prediction of the oxygen vacancy trends and

*Corresponding author email: bhethana@usf.edu

the stability of the samples were corroborated by the ~~temperature~~ temperature-programmed reduction and oxidation reactions and in-situ XRD crystallography.

1. Introduction:

The environmental and energy scenario of the world has resulted in active research towards recycling carbon dioxide.[1, 2] Carbon capture, utilization and sequestration (CCUS), an advanced methodology in comparison to only carbon capture and sequestration (CCS) has garnered a lot of attention recently.[3] In this pursuit, the chemical route of fixing carbon dioxide to hydrocarbon fuels has been quite popular.[2] Among the different existing protocols, the solar thermochemical approach has been of prime focus, for natural reasons of utilizing the vast abundance of solar power in the process.[4-9] A recent analysis of the feasibility and the potential of various solar-to-fuel processes by Mallapragada et al. revealed the thermochemical route to be the most viable option as well.[10] There are reports of successful thermochemical carbon dioxide conversion using concentrated solar energy to account for the high temperature requirements of the process.[6, 9, 11]

The thermochemical conversion of carbon dioxide works in a simple two-step process, wherein, the first step involves the creation of oxygen deficient metal oxides by heating the materials at high temperature under inert conditions. In the subsequent second step, carbon dioxide flown over these oxygen vacant reduced materials is dissociated to carbon monoxide and the metal oxides get replenished of their lost oxygen. The success of this cyclic operation between stoichiometric and oxygen deficient materials for the conversion of carbon dioxide is dependent on the stability of the materials at both the stoichiometric and oxygen deficient conditions at high temperatures. Water splitting for the generation of hydrogen by similar thermochemical principle has been studied as well, wherein the water vapor is passed instead of

*Corresponding author email: bhethana@usf.edu

carbon dioxide and thus, obtaining hydrogen instead of carbon monoxide.[9] The conceptual picture of thermochemical carbon dioxide conversion is shown in Figure 1. Carbon dioxide conversion, in general, has been found limited by the high temperature requirement and the scarcity of materials that can suffice the requirements of the thermochemical CO_2 splitting to CO. This situation has led to the origin of a modified carbon dioxide conversion cycle, wherein the reduction step is done in the presence of hydrogen, to produce more oxygen vacancies at lower temperatures. The second step of carbon monoxide production from carbon dioxide remains similar. This process of Reverse Water Gas Shift - Chemical Looping (RWGS-CL) has been found successful as studied by Daza et al.[12, 13] In general, the feasibility of the thermochemical and RWGS-CL processes is governed by the oxygen vacancy formation characteristics of the metal oxide. Amongst them, ceria and perovskite oxides are known to exhibit good oxygen vacancy characteristics. One of theA pioneering works on thermochemical carbon dioxide conversion was reported using ceria.[6] Subsequently, there were reports of success with the use of perovskite oxides and perovskite oxides on various supports.[9, 11, 14] Perovskite oxides are a class of mixed metal oxides of the form ABO_3, being used in applications like dielectrics, catalytic reactions, adsorbents, membranes, solid oxide fuel cells.[15-18] Thermal stability of these materials, and stability in non-stoichiometric conditions are some of the few properties that make them so interesting.[19, 20]
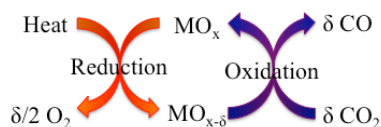

Figure 1. General schematic of the thermochemical process

Carbon dioxide conversion is strongly correlated to extent of oxygen vacancy formation and the material's keenness to regain its lost oxygen. Reduction temperature of the material is

Comment [KJ1]: Mention spinels too maybe for completeness...

*Corresponding author email: bhethana@usf.edu

thus, an important parameter to look out for, as it represents the energy cost for oxygen vacancy formation and in the process perspective, it also reflects the cost of CO_2 conversion cycles. This property is closely related to the particular material composition. The oxygen vacancy characteristic is thus an intrinsic property of the material itself. Perovskite oxides provide a vast opportunity for tuning the material properties by substituting appropriate elements in their respective 'A' and 'B' sites of ABO_3 type crystal structure. There have been reports of varying oxygen vacancy formation and lowering the reduction temperature via material composition tuning.[13, 21] The oxygen vacancy formation characteristics are probed experimentally as the extent of oxygen vacancy formation, the onset and peak temperature of vacancy formation and computationally as the energy of oxygen vacancy formation at different vacancy concentrations. Considerable theoretical efforts have been expended in recent years to obtain optimum candidates for the thermochemical conversion by calculating oxygen vacancy formation energy using density functional theory.[22-24] The lanthanum based perovskite oxides have been found to work well for these processes.[9, 12, 13, 23] The effects of strontium substitution in 'A' site and manganese and aluminum composition in 'B' site have been reported by Deml et al.[23] Screening across a range of transition metals has also been done to find the optimum perovskites to be used for this purpose.[24] Probing the energy of oxygen vacancy formation in the bulk is thus an important route for predicting the appropriate material for the carbon dioxide conversion processes. However, the carbon dioxide adsorption, dissociation and desorption of CO occur only at the surface of the materials. Hence, a critical understanding of the surface structure, stability, and reactions is important as well. These perovskite oxides can exhibit different surface terminations. It is thus, relevant to know which surface terminations are more probable to be present in nature, which of them are more likely to accommodate oxygen vacancies in

*Corresponding author email: bhethana@usf.edu

experimental conditions and most importantly which of them exhibit the ideal sites for CO_2 conversion reactions. With the recent knowledge of synthesis protocols for growth of preferred crystal facets and terminations in perovskites and double perovskites,[25-28] prediction of the best sites on these perovskite materials towards CO_2 conversion materials becomes more pertinent.

This article is focused on the bulk oxygen formation characteristics and surface oxygen vacancy characteristics of $La_{(1-x)}Sr_xFe_{(1-y)}Co_yO_{(3-\delta)}$ with x = 0.25 or 0.5 and y = 0 or 0.5 or 1. The most stable bulk crystal structures of $La_{0.5}Sr_{0.5}BO_3$ and $La_{0.75}Sr_{0.25}BO_3$ with B = Co or Fe or $Fe_{0.5}Co_{0.5}$ are predicted. Along with the investigations on oxygen vacancy formation energies with varying 'A' site and 'B' site compositions, dependence of vacancy formation on the different sites of bulk materials has been reported as well. The theoretical trends are corroborated by the ~~temperature~~ temperature-programmed reduction of the perovskites both in inert and hydrogen environment. The materials exhibited great stability in oxygen deficient conditions as predicted by theoretical trends. Although, there have been several studies on the strontium segregation on perovskite type oxides based on XPS, XAS and LEIS studies and computational techniques,[29-32] a rigorous analysis of the various terminations is absent. A detailed study is, hence, performed to probe the stability of the pure stoichiometric surface terminations along the <100> and <110> directions. Oxygen vacancy formation tendencies on these different terminations are henceforth examined to predict the surface terminations that are more likely to exhibit oxygen vacancies. Finally, the effect of these terminations, both in pure conditions and in oxygen deficient conditions, on carbon dioxide conversion has been studied by calculating the carbon dioxide adsorption strengths on the different surface terminations along (100) crystal planes of $La_{0.5}Sr_{0.5}FeO_3$. The most potent surface terminations that can convert carbon dioxide are thus predicted. This is based on the concept of using suitable descriptors for probing

*Corresponding author email: bhethana@usf.edu

reactions and finding desired materials for the same as had been reported in literature.[33-35] A recent work has also revealed the correlation of carbon dioxide conversion performance with carbon dioxide adsorption strengths.[13] Overall, this study is an effort for better understanding of the material dependent oxygen evolution process and to highlight the importance of surface terminations for accurate prediction of oxygen vacancy formation in experimental conditions and carbon dioxide conversion on the preferred surfaces of these perovskite oxides.

2. Computational Methods:

Density functional theory (DFT) based calculations are done using Vienna ab initio Simulation Package (VASP – 5.2.8).[36-40] All the calculations used plane wave basis set and gradient generalization for the approximation of the electron densities. The core electronic states are treated by projector augmented wave (PAW) potentials[41, 42] and Perdew Wang -91(PW-91)[43] variant of exchange correlation. Consistent use of default potentials for lanthanum, strontium, iron and cobalt are done while soft potentials are used for oxygen potentials. Throughout the study, a constant energy cut off of 500 eV has been used. The convergence criterion for the ionic relaxations is set at 0.001eV/atom. All the bulk phase systems studied are cubic, with 5 atoms in a unit cell and 40 atoms in a $2\times2\times2$ supercell, while 80 atoms containing surface slabs are made of $2\times2\times4$ supercells with 15 Å of vacuum along surface direction to mimic the absence of atomic periodicity on surfaces. Convergence with respect to the k point sampling has been checked; finally, calculations for all the 40 atom supercell of bulk stoichiometric and non-stoichiometric perovskites are done with $4\times4\times4$ k point mesh generated by an automatic scheme having Monkhorst Pack grid. Magnetic effects are not considered explicitly as it was known to have

*Corresponding author email: bhethana@usf.edu

minor effects in the systematic trends of energy.[24] For the slab calculations of the surface structures, dipole correction has been accounted.[44]

The initial ground state configurations for each of the materials are obtained through a series of varying cell volume calculations. Once the ground state lattice constant is established, the entire set of parameters are used for the nonstoichiometric calculations as well. Though oxygen vacancy formation in a material is a complex process consisting of several steps, the major energy intensive step is the dissociation of the metal-oxygen bond. Hence, computational oxygen vacancy formation energies calculated as enthalpy difference between the initial stoichiometric material and the final oxygen deficient material along with gas phase oxygen mostly represents the energy barrier for the dissociation of the metal-oxygen bonds and the subsequent relaxation of the oxygen deficient structure. The creation of oxygen vacancies is marked by systematic removal of oxygen atoms, either from bulk or surface. The extent of oxygen vacancy (δ) is defined as oxygen deficiency per unit molecule of ABO_3; thus in a 40 atom supercell of perovskites, $\delta = 0.125$ and 0.25 are marked by removal of one oxygen atom and two oxygen atoms respectively. For surface oxygen vacancies of $\delta = 0.125$ and 0.25, the number of oxygen atoms removed from the 80 atom supercell were two and four respectively. The oxygen vacancy formation energy is calculated as per equation 1.

$$E_{vac} = E_{ABO_{(3-\delta)}} + \delta \times \frac{n}{2} E_{O_2} - E_{ABO_3} \dots\dots [1]$$

where, E_{ABO_3} is the total energy of the pure stoichiometric perovskite supercell having n unit cells, while $E_{ABO_{(3-\delta)}}$ is that of the oxygen vacant perovskite supercell, 'n' representing the number of unit cells considered (8 for bulk calculations and 16 for surface calculations) and E_{O_2} is the molecular energy of oxygen. All the oxygen vacancy formation energies (E_{vac}/n) are expressed as energy to create 'δ amount of oxygen vacancy' per ABO_3. The oxygen over-binding

*Corresponding author email: bhethana@usf.edu

error has been addressed by Wang et al for PBE functionals by using a correction factor of 1.36 eV.[45] The correction factor for PW-91 (O_s) functional has been calculated to be 0.33 eV by Lee et al.[46] All the calculations of oxygen vacancy formation energy has been corrected by this factor. The oxygen vacancy formation energies were also calculated using DFT+U to account for the Hubbard U correction for the transition metals on the B sites. The carbon dioxide adsorption energy on the materials is reported based on equation 2.

$$E_{ads} = E_{P+CO_2} - E_{CO_2} - E_P \dots\dots [2]$$

where, E_P is the energy of either pure or oxygen vacant perovskite, E_{P+CO_2} is the energy of combined system of CO_2 adsorbed on the perovskite while E_{CO_2} is the energy of molecular gaseous CO_2.

Charge density analysis was done to probe the surface terminations and the various oxygen removal sites. Charge associated with an atom has been calculated using the Bader charge analysis code by Henkelman et al.[47-49] The charge density plots were done using VESTA.[50]

3. Experimental Methodology:

The $La_{0.75}Sr_{0.25}Fe_{(1-y)}Co_yO_3$ (y= 0, 0.5 and 1) ~~and La~~$_{0.5}$~~Sr~~$_{0.5}$~~CoO~~$_3$ samples were synthesized by the Pechini method, as described previously.[12] ~~The crystalline structure of the samples was characterized by X-ray diffraction (XRD)~~ The~~and the~~ oxygen vacancy formation under inert (He) and hydrogen (10% H_2/He) ~~atmospheres~~ were measured by temperature-programmed oxygen vacancy formation (TPOvac), and temperature-programmed reduction (TPR), respectively, from room temperature to 950 °C. All experimental elements are described elsewhere in detail.[51] Final calcination (synthesis) temperature of the samples used in the TPOvac and

*Corresponding author email: bhethana@usf.edu

TPR experiments were 750 °C[12] and 950 °C[13] respectively. ~~The samples used in the TPOvac experiments were charred at 750 °C[12], whereas the ones used in the TPR experiments were charred at 950 °C.[13]~~ The stability of the crystal structures of the La$_{0.75}$Sr$_{0.25}$CoO$_3$ (calcined at 750 °C) oxide~~samples~~ while heating under an inert atmosphere was~~ere~~ tested via in situ X-ray diffraction using a Bruker D8 ~~advance~~ X-Ray D~~d~~iffractometer with Cu Kα (λ=0.154 nm)~~K$_α$~~ at a heating rate of 25 ° C/min. The experimental elements of the in situ XRD can also be found elsewhere in more detail. [12]

Three RWGS-CL experiments ~~anode~~were performed on the La$_{0.75}$Sr$_{0.25}$FeO$_3$ (calcined at 950 °C). In these experiments, the sample was heated in He to 550 °C and was reduced for 3, 13 or 17 min in 10% H$_2$/He. After 20 min of He flow, CO$_2$ was introduced (10% CO$_2$/He) until CO was no longer produced. Further experimental details can be found elsewhere. [13] The results for amount of H$_2$O produced during H$_2$-reduction and CO produced during CO$_2$ flow are quantified in Figure 12.l.

4. Results and Discussions:

4.1. Bulk crystal structure:

La$_{0.75}$Sr$_{0.25}$Fe$_{(1-y)}$Co$_y$O$_3$ (y = 0, 0.5 and 1) and La$_{0.5}$Sr$_{0.5}$CoO$_3$ samples, as prepared by the Pechini method, revealed the presence of mixed crystalline phases with a predominance of cubic phase. Although, the diffraction pattern revealed the general crystallographic structures, it was unable to provide the details of the elemental organization within the structure itself. The local distribution of the ions is expected to have effects on the electronic and charge distribution within the material. Hence, a systematic study over a set of plausible bulk phase configurations has been conducted via theoretical calculations. Only the cubic phase has been the focus of this study as cubic phase was found prevalent experimentally. Furthermore, the different crystalline phases of perovskite oxides like orthorhombic, tetragonal and hexagonal tend to shift to high

*Corresponding author email: bhethana@usf.edu

symmetry configurations like the cubic phase at the high temperatures.[52, 53] Since, the thermochemical reaction temperatures are also high enough ($\sim 1000^{\circ}$ C and above), it is quite justified to accept cubic phase as the system of study. Moreover, the trends of oxygen vacancy formation were found invariant to the bulk phase structure of the material.[24] Within these high symmetry cubic phases (space group Pm3m), the lattice organization of the individual 'A' and 'B' site elements led to the generation of several configurations. Figure S1 shows a few possible bulk phase cubic configurations of $La_{0.5}Sr_{0.5}FeO_3$, made through a random distribution of lanthanum and strontium atoms in a supercell of 40 atoms having 4 atoms of lanthanum, 4 atoms of strontium, 8 atoms of iron and 24 atoms of oxygen. The configuration having the least energy, as calculated by density functional theory, was chosen to be the most stable one. The stable configurations of all the six samples (various La:Sr and Co:Fe ratios) are shown in Figure 2. The stable configurations of $La_{0.5}Sr_{0.5}BO_3$ (B=Fe or Co or $Fe_{0.5}Co_{0.5}$) revealed the preference for alternate layering of lanthanum and strontium atoms (as shown in configuration (a) in Figure S1 and Figures 2(a-c)) while, all the stable configurations of $La_{0.75}Sr_{0.25}BO_3$ (B=Fe or Co or $Fe_{0.5}Co_{0.5}$) showed tendency to form linear chains of strontium surrounded by lanthanum layers as shown in the Figures 2(d-f). A gradual increase of cell volume with the replacement of cobalt with iron on the 'B' site is evident from the increase in lattice constants (Table 1).

(a) $La_{0.5}Sr_{0.5}CoO_3$	(b) $La_{0.5}Sr_{0.5}FeO_3$	(c) $La_{0.5}Sr_{0.5}\,Fe_{0.5}Co_{0.5}O_3$

*Corresponding author email: bhethana@usf.edu

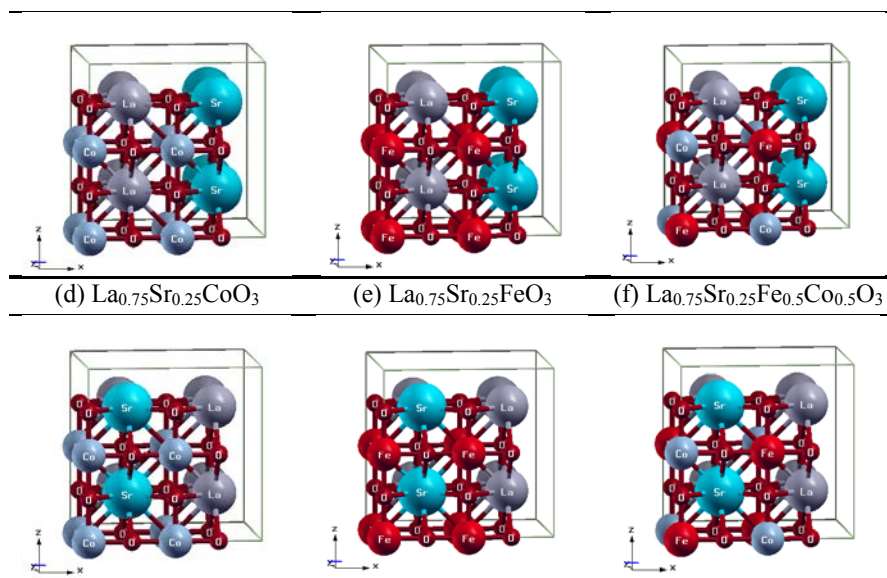| (d) $La_{0.75}Sr_{0.25}CoO_3$ | (e) $La_{0.75}Sr_{0.25}FeO_3$ | (f) $La_{0.75}Sr_{0.25}Fe_{0.5}Co_{0.5}O_3$ |

Figure 2. Most stable bulk phase configurations of $La_{(1-x)}Sr_xFe_{(1-y)}Co_yO_{(3-\delta)}$

Table 1. Lattice constants of $La_{(1-x)}Sr_xFe_{(1-y)}Co_yO_{(3-\delta)}$

Material	a (Å)	Material	a (Å)
$La_{0.5}Sr_{0.5}CoO_3$	3.835	$La_{0.75}Sr_{0.25}CoO_3$	3.835
$La_{0.5}Sr_{0.5}Fe_{0.5}Co_{0.5}O_3$	3.8435	$La_{0.75}Sr_{0.25}Fe_{0.5}Co_{0.5}O_3$	3.8535
$La_{0.5}Sr_{0.5}FeO_3$	3.857	$La_{0.75}Sr_{0.25}FeO_3$	3.8695

4.2. Bulk Oxygen Vacancies:

~~One of the~~A crucial factor~~s~~ that governs the carbon dioxide reduction in thermochemical cycles is the extent of oxygen vacancies. Oxygen vacancy formation energy provides insights into the ease of oxygen removal and oxygen refilling. The trends of the oxygen vacancy formation energy for the bulk system of $La_{(1-x)}Sr_xFe_{(1-y)}Co_yO_3$ for different extents of oxygen vacancies (δ = 0.125, 0.25 and 0.375) are portrayed in Figure 3a. A systematic trend was observed for the composition dependent oxygen vacancy generation. It was found easier with increasing strontium in the 'A' site and decreasing iron content in the 'B' site as revealed in

*Corresponding author email: bhethana@usf.edu

Figure 3b; this trend is in support of earlier reports as well.[23] This aspect is also corroborated experimentally for the $La_{0.75}Sr_{0.25}Fe_{(1-y)}Co_yO_3$ samples as shown in Figure 4a. For both the TPOvac and TPR experiments, iron-rich materials exhibit lower oxygen vacancy formation, that too at higher peak temperatures, thus indicating a higher energy barrier for oxygen vacancy generation. Quantification of the H_2O/ABO_3 produced during TPR experiments was done from room temperature to 600 °C. The trend of oxygen vacancy formation energies with varying B sites is revealed in Figures S2, when the calculations were done using DFT+U, with U values of 2, 3 and 4 for the B site elements.

(a)　　　(b)
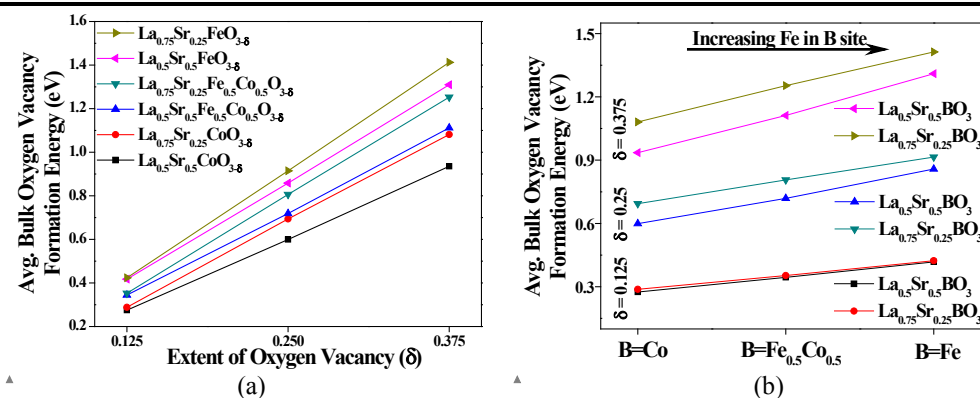
Figure 3. Bulk oxygen vacancy trends in $La_{(1-x)}Sr_xFe_{(1-y)}Co_yO_{(3-\delta)}$ for $\delta = 0.125$, 0.25 and 0.375

Formation of higher extents of oxygen vacancy is expected to have higher energy requirements (as revealed in Figure 3a), but the exciting aspect being revealed was that the energy cost scales almost linearly with the extent of oxygen vacancy (Figure 3a). This result suggests suggested a significant stability of the materials under high oxygen vacant conditions. Being stable at higher oxygen vacancies and not decomposing to other compounds is an essential requirement for the successful operation of this carbon dioxide conversion process. This aspect is also corroborated in Figure 4b for the $La_{0.75}Sr_{0.25}CoO_3$ sample. Monitoring the crystalline structure evolution during the formation of oxygen vacancies (Figure 4b), demonstrateds the

*Corresponding author email: bhethana@usf.edu

stability of the cubic crystalline structure. The XRD ~~profile~~ lines ~~shifts~~ shifted to lower $2\theta°$ as the temperature is increased, due to the expansion of the lattice. The lowest $2\theta°$ values are achieved at the peak O_2 evolution temperature. As the sample cools, it returns to its original state, upon re-oxidation of the structure.
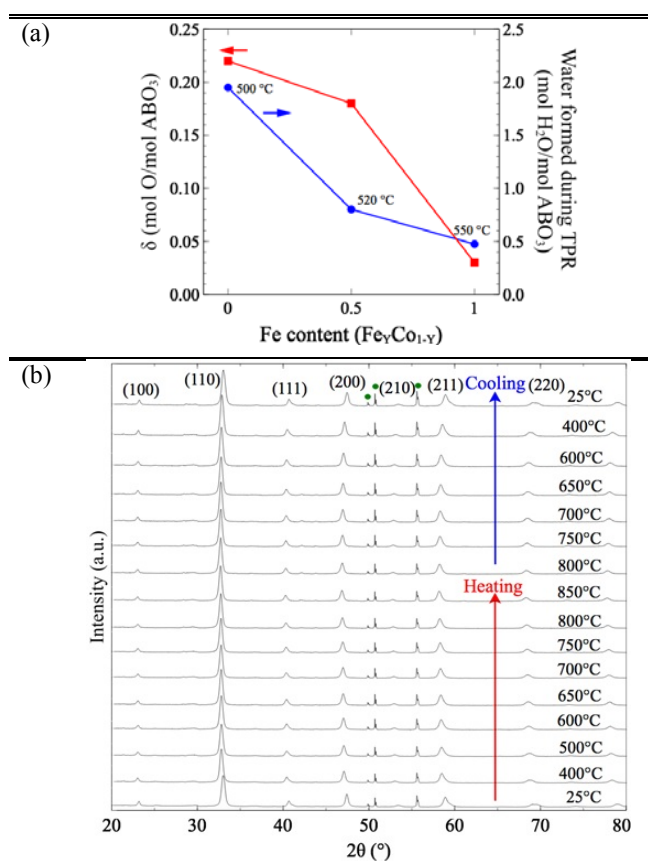

Figure 4. (a) Ratio of oxygen removal from the $La_{0.75}Sr_{0.25}Fe_{(1-y)}Co_yO_3$ (y=0, 0.5 and 1) samples under inert environment (left) and under 10% H_2/He (right). In the TPR experiments, the H_2O removed was quantified up to 600 °C, and the numbers represent the peak reduction temperature for the quantified area. (b) In-situ XRD of the cubic $La_{0.75}Sr_{0.25}CoO_3$ (x=0.25, y=1) under 50 sccm of He. The sample was heated from room temperature to 850 °C at 25 °C/min and cooled

*Corresponding author email: bhethana@usf.edu

back to room temperature. The diffraction lines at 50, 51 and 55 2θ° are due to the quartz sample holder.

A systematic study of the site specific oxygen vacancy formation was also conducted. Studies of oxygen mobility or transport are dependent on cation ordering and thus, on the site specificity of oxygen vacancy generation as well.[54, 55] Table 2 lists the site specific oxygen vacancy energies for $La_{0.5}Sr_{0.5}BO_3$.

Table 2: Site specificity of oxygen bulk oxygen vacancy

Material Name	Extent of oxygen vacancy (δ)	Oxygen vacancy formation energy (eV)	
		in La Layer	in Sr Layer
$La_{0.5}Sr_{0.5}CoO_3$	0.125	0.2483 ~~1.9863~~	~~2.5527~~ 0.3191
	0.25	0.5553 ~~4.4422~~	~~5.3438~~ 0.6680
	0.375	0.8712 ~~6.9693~~	~~8.0427~~ 1.0053
$La_{0.5}Sr_{0.5}Fe_{0.5}Co_{0.5}O_3$	0.125	~~2.6038~~ 0.3255	~~3.0759~~ 0.3845
	0.25	~~5.3499~~ 0.6687	~~6.3215~~ 0.7902
	0.375	~~8.2997~~ 1.0375	~~9.5265~~ 1.1908
$La_{0.5}Sr_{0.5}FeO_3$	0.125	~~3.1937~~ 0.3992	~~3.6048~~ 0.4506
	0.25	~~6.6204~~ 0.8276	~~7.4049~~ 0.9256
	0.375	1.2299 ~~9.8392~~	~~11.0438~~ 1.3805

For all the different extents of oxygen vacancies, oxygen removal from the lanthanum layer was much favorable to that from a strontium layer. An oxygen atom being removed from a lanthanum layer and a strontium layer involves breaking the electronic interactions of the oxygen atom with the neighboring 'A' site and 'B' site atoms. Removal of a neutral oxygen atom from a B-O bond leaves the electron cloud of B free to redistribute across the nearby atoms. Thus, not only the B site elements change their oxidation states, but the nearby oxygen atoms and 'A' site elements

*Corresponding author email: bhethana@usf.edu

get a share of the electron cloud by the inductive effect. While the presence of d orbitals in lanthanum can make it easier to accommodate the electrons, its smaller ionic radius makes it also exhibit a lesser screening effect than strontium and hence allows for a better charge flow across the lattice. Charge analysis based on Bader's method, revealed a much stronger effect on the nearby B site atoms, when a vacancy is generated in the strontium layer. Charge transfer was found much easier in the lanthanum layer. Hence, when a vacancy is formed in the lanthanum layer, the electron cloud gets re-distributed across the lanthanum layer easily. While in the strontium layer, the charge transfer was not favorable in the strontium layer itself resulting in higher charge accumulation on the B site atoms which further affects the neighboring lanthanum layer. This energy cost of electron re-distribution in the strontium layer makes it harder for oxygen vacancy creation in that layer. The charge density difference plots between the pure and oxygen vacant structures for $La_{0.5}Sr_{0.5}FeO_3$ and $La_{0.5}Sr_{0.5}CoO_3$ are shown in Figure 5 (a-d). Studies on double perovskites have shown the effect of cation ordering and site preference towards oxygen vacancy formation.[54, 56]

$\delta=0.125$ vacancy in lanthanum layer	$\delta=0.125$ vacancy in strontium layer
$La_{0.5}Sr_{0.5}FeO_3$	
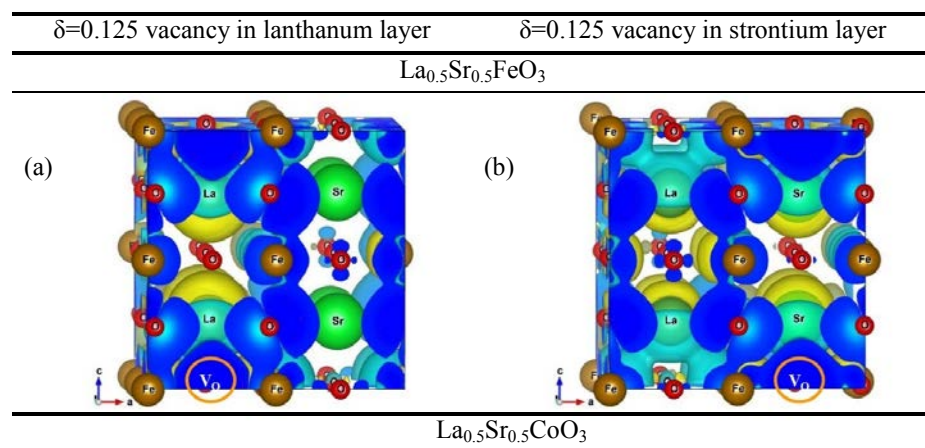
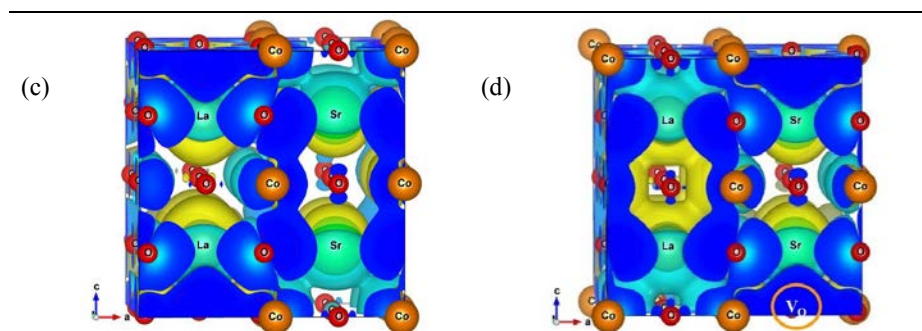| $La_{0.5}Sr_{0.5}CoO_3$ | |

*Corresponding author email: bhethana@usf.edu

Figure 5. Charge density difference maps for the oxygen removal from lanthanum-rich and strontium layers of (a-b) $La_{0.5}Sr_{0.5}FeO_3$ and (c-d) $La_{0.5}Sr_{0.5}CoO_3$
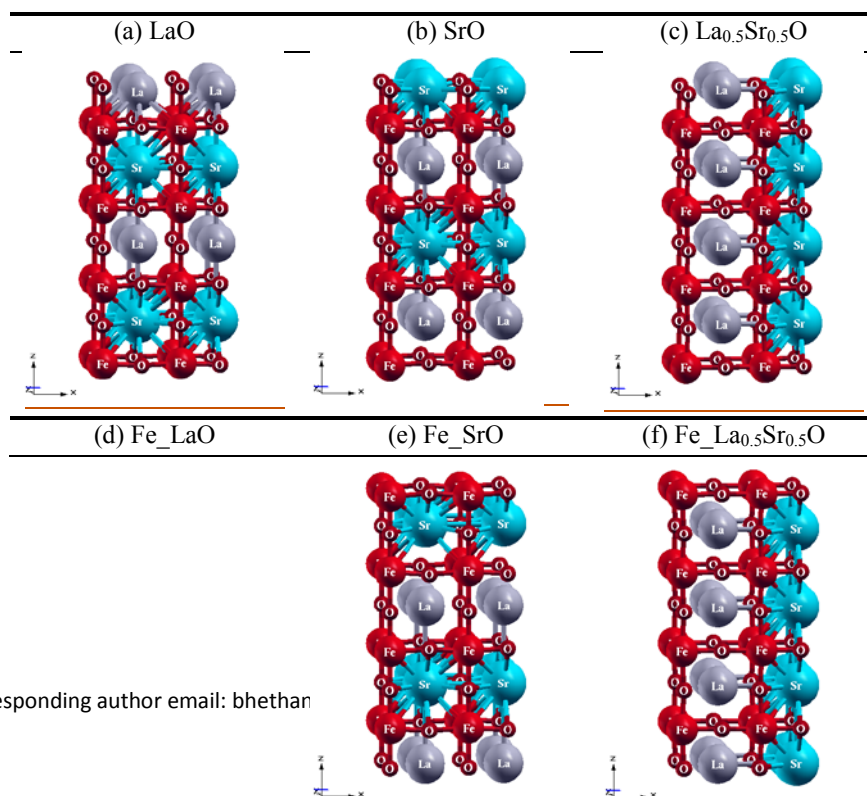
Apart from these, we could also find that a series of oxygen vacancies, producing a 'vacancy tunnel' like structure, was more favorable than a random distribution of oxygen vacancies throughout the material. There have been reports of similar stable row vacancies in brownmillerite type of structure.[57-59] For both the lanthanum-rich layer and strontium-rich layer of $La_{0.5}Sr_{0.5}FeO_3$, randomly distributed oxygen vacancy formation was found to have ~0.5 eV higher energy barrier than a continuous vacancy tunnel formation. Oxygen vacancies along a row of 'B-O' axis and concentrated vacancies around B site metals are also favored. Figure S32 reveals the energy of vacancy tunnel formation and random vacancy creation in the bulk $La_{0.5}Sr_{0.5}FeO_3$ material along with their respective charge density difference plots. Other materials like $La_{0.5}Sr_{0.5}CoO_3$ and $La_{0.5}Sr_{0.5}Fe_{0.5}Co_{0.5}O_3$ also exhibit similar trends.

4.3. Surface structure:

The different crystal facets present in $La_{(1-x)}Sr_xFe_{(1-y)}Co_yO_3$ were revealed in the XRD study.[13] The two major crystallographic planes prevalent were (100) and (110). Mixed perovskite oxides of this nature behold the possibility of exhibiting various surface terminations along these planes, based on the elemental presence on those surface terminations. Probing the different

*Corresponding author email: bhethana@usf.edu

surface terminations and their role towards the thermochemical reactions of interest was hence important. For the materials of focus, $La_{(1-x)}Sr_xFe_{(1-y)}Co_yO_3$, six different terminations were found to exist along the (100) facets of both $La_{0.5}Sr_{0.5}BO_3$ and $La_{0.75}Sr_{0.25}BO_3$ where 'B' stands for the different 'B' site components like Fe or Co or $Fe_{0.5}Co_{0.5}$. These six surface terminations were broadly classified into two major groups: 'AO' terminations (surfaces having an atomic layer of 'A' site metal and oxygen on the surface) and 'BO' terminations (surfaces having an atomic layer of 'B' site metal and oxygen on the surface). Each of these two classes has three variations based on the A site composition on the surface or in the immediate sub-surface. For the 'AO' surface terminations of $La_{0.5}Sr_{0.5}BO_3$, the three variations of 'A' composition were (i) only lanthanum, (ii) lanthanum and strontium with 1:1 ratio (or $La_{0.5}Sr_{0.5}$) and (iii) only strontium. Similarly, the 'AO' compositions for $La_{0.75}Sr_{0.25}BO_3$ were (i) only lanthanum (ii) lanthanum and strontium in a ratio of 3:1 (or $La_{0.75}Sr_{0.25}$) and (iii) lanthanum and strontium with 1:1 ratio (or $La_{0.5}Sr_{0.5}$).

(a) LaO   (b) SrO   (c) $La_{0.5}Sr_{0.5}O$

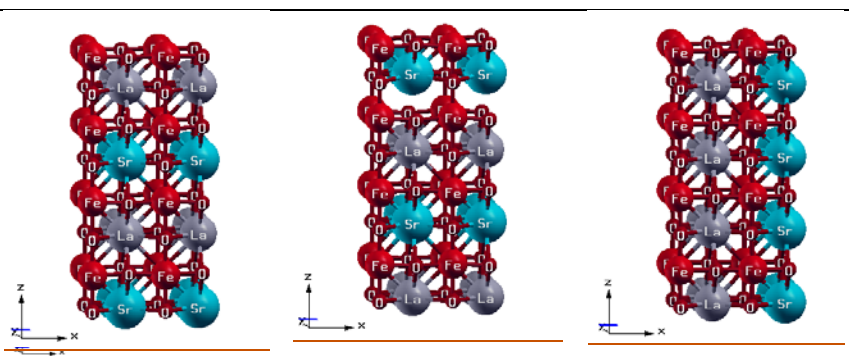(d) Fe_LaO   (e) Fe_SrO   (f) Fe_$La_{0.5}Sr_{0.5}O$

*Corresponding author email: bhethan

Figure 6(a-f): Various surface termination along (100) facets of $La_{0.5}Sr_{0.5}FeO_3$

The different 'BO' surfaces were classified based on the different 'AO' composition that lies in the immediate sub-surface. The nomenclature of the 'AO' surfaces was thus, made according to the initials of the composition and that for 'BO' surfaces was done as per B-atop-AO-sub-layer or in short B_AO. The representative structures for these six surface terminations along (100) cubic facets of $La_{0.5}Sr_{0.5}FeO_3$ are shown in Figure 6(a-f).

Theoretical studies on the stability of these surfaces are shown in Figures 7a and 7b. A trend of stability was seen amongst the six different surface terminations along (100) surfaces of $La_{0.5}Sr_{0.5}BO_3$ and $La_{0.75}Sr_{0.25}BO_3$. For the 'AO' terminations, higher content of strontium exposed to the surface was preferred in comparison to lanthanum. The orders of stability for 'AO' terminations in $La_{0.5}Sr_{0.5}BO_3$ and $La_{0.75}Sr_{0.25}BO_3$ materials are thus: $SrO > La_{0.5}Sr_{0.5}O >$ LaO and $La_{0.5}Sr_{0.5}O > La_{0.75}Sr_{0.25}O >$ LaO, respectively. This result is in accord with several studies that demonstrate strontium segregation to the surface.[30, 32, 60] Experimental investigation by Druce et al. supports this result, although it relates this feature not only to simple surface relaxation, but an extensive surface reconstruction.[32] On the other hand, the stability of the 'BO' terminations is related to the composition of 'AO' layer in the sub-surface. Increasing the

*Corresponding author email: bhethana@usf.edu

strontium content in the immediate sub surface tends to destabilize the 'BO' surface termination. Hence, the orders of stability for 'BO' termination for $La_{0.5}Sr_{0.5}BO_3$ and $La_{0.75}Sr_{0.25}BO_3$ materials are as: B_LaO > B_La$_{0.5}$Sr$_{0.5}$O > B_SrO and B_LaO > B_La$_{0.75}$Sr$_{0.25}$O > B_La$_{0.5}$Sr$_{0.5}$O, respectively. Amongst all the six surface terminations, the 'AO' termination having the highest strontium content proved to be the most stable. This stability pattern was valid for all the materials irrespective of the B site composition (Fe or Co or $Fe_{0.5}Co_{0.5}$) as is evident from Figures 7a and 7b.

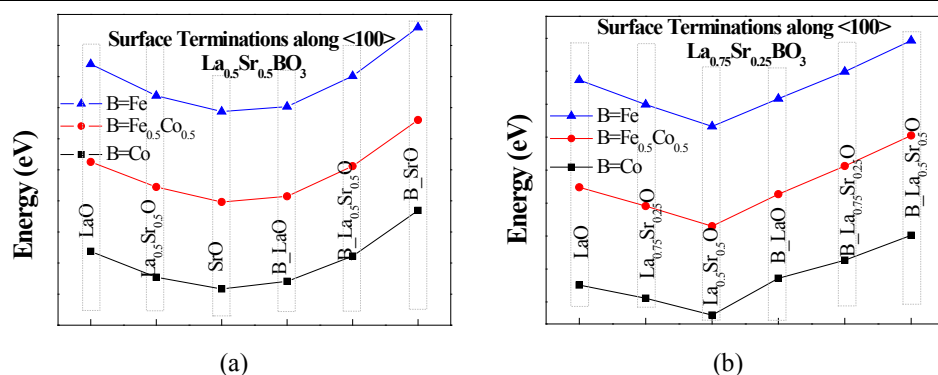Figure 7. Stability of the surface terminations along (100) crystal planes for (a) $La_{0.5}Sr_{0.5}BO_3$ and (b) $La_{0.75}Sr_{0.25}BO_3$ [B = Co, $Fe_{0.5}Co_{0.5}$ and Fe]

Charge density analyses for these surface terminations were conducted for interpretation of the stability trends. For $La_{0.5}Sr_{0.5}FeO_3$, the stability of SrO surface termination over LaO termination was explained by the lower charge density of surface strontium ions (0.163 e/Bohr^3) than that of lanthanum ions (0.232 e/Bohr^3) on the surface of LaO termination. The charge density of the surface 'B' atoms and the oxygen atoms were similar for all the BO terminations. Hence, the stability among the BO terminations was better addressed by the interlayer Coulombic interactions. The surface charge density on the iron ions was calculated to be 0.48 e/Bohr^3, while that for lanthanum and strontium ions were 0.232 e/Bohr^3 and 0.163 e/Bohr^3

*Corresponding author email: bhethana@usf.edu

respectively. Fe_LaO termination has an iron-rich surface layer with lanthanum ions in the immediate sub-surface, while the sub-surface of Fe_SrO termination has strontium ions. Coulomb repulsion between the surface and sub surface layers being proportional to the product of the charge of the ions present on those surfaces, it is stronger between an iron-rich surface layer and a lanthanum-rich sub layer than that between an iron-rich surface layer and a strontium-rich sub layer. This accounts for more interlayer surface relaxation in Fe_SrO termination while less relaxation in Fe_LaO termination. This energy cost for more relaxation makes the Fe_SrO surface termination less preferred than Fe_LaO termination. The extent of relaxation in the top most surface is documented in Table 3.

Table 3: Relaxation in the top layer of a few (100) surface terminations of $La_{0.5}Sr_{0.5}FeO_3$

Relaxation in the top most layer	(100) Surface Terminations of $La_{0.5}Sr_{0.5}FeO_3$			
	LaO	SrO	Fe_LaO	Fe_SrO
Absolute value (pm)	5.366	9.679	6.255	10.252
% of the bulk interlayer distance	2.82	4.96	3.28	5.25

Similarly, the different terminations that are formed along (110) crystal facet are 'ABO' termination (having both the A site and B site components along with oxygen on the surface) and 'O' termination (having only oxygen on the surface lying atop the 'ABO' sub-surface). For $La_{0.5}Sr_{0.5}BO_3$, the only 'ABO' surface termination was $La_{0.5}Sr_{0.5}BO$ and the only 'O' layer is oxygen-atop-$La_{0.5}Sr_{0.5}O$ or simply O_ $La_{0.5}Sr_{0.5}BO$. For $La_{0.75}Sr_{0.25}BO_3$, however, there are two types of 'ABO' terminations (LaBO and $La_{0.5}Sr_{0.5}BO$) based on the compositional variation of 'A' elements in the 'ABO' layer and hence the two 'O' terminated surfaces are O_LaBO and O_ $La_{0.5}Sr_{0.5}BO$. The two terminations along (110) planes of $La_{0.5}Sr_{0.5}FeO_3$ are shown in Figure

*Corresponding author email: bhethana@usf.edu

S~~43~~(a-b) and the terminations along (110) facets of $La_{0.75}Sr_{0.25}FeO_3$ are shown in Figure S~~43~~(c-f).

The stability of the surface terminations along (110) planes [Figures 8 (a-b)] were found to be dependent on the B site composition. In general, 'O' terminations were more stable than the 'ABO' terminations. For $La_{0.5}Sr_{0.5}BO_3$, the preference of 'O' termination becomes more pronounced with the increase of iron content in the B site. For $La_{0.5}Sr_{0.5}CoO_3$, the two terminations are almost equally stable. For $La_{0.75}Sr_{0.25}BO_3$, the most stable termination was O_LaBO, its preference increasing with increased iron content in the 'B' site. For $La_{0.75}Sr_{0.25}CoO_3$, the O_LaCoO terminated surface exhibited almost similar stability as the $La_{0.5}Sr_{0.5}CoO$ terminated one. Between the two 'O' terminations, the stability was governed by the sub surface 'ABO' layer as is shown in Figure 8b. Comparison amongst the absolute energies of the two sets of (100) and (110) surface terminations for all the six materials, predicted easy formation of (100) crystal facets over (110).
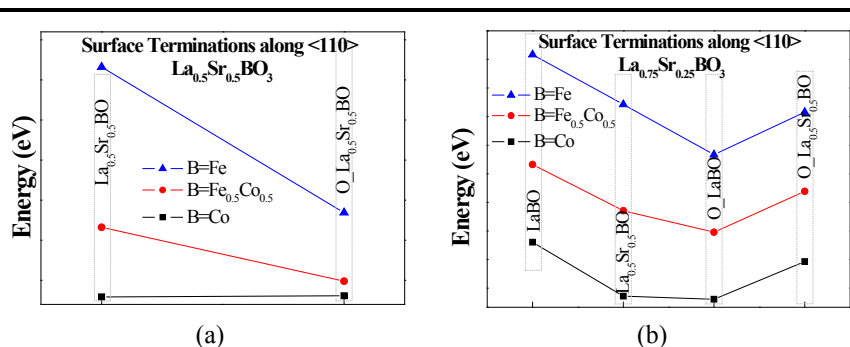

(a)   (b)

Figure 8. Stability of the surface terminations along (110) crystal planes for (a) $La_{0.5}Sr_{0.5}BO_3$ and (b) $La_{0.75}Sr_{0.25}BO_3$ [B = Co, $Fe_{0.5}Co_{0.5}$ and Fe]

These surface terminations are of particular interest as these are the most potent candidates to be generated in experimental conditions, both in stoichiometric and oxygen deficient states, and it is on these surfaces that the carbon dioxide conversion reactions occur.

*Corresponding author email: bhethana@usf.edu

4.4. Surface Oxygen Vacancies:

Most of the catalytic reactions on oxygen deficient materials occur at or in the vicinity of the surface oxygen vacancy based active sites.[61-66] Hence, a detailed investigation of the oxygen vacancies on the various surface terminations along (100) and (110) planes was conducted. The slab model for surfaces had 80 atoms. Hence, to create a vacancy of $\delta = 0.125$ and 0.25, two and four oxygen atoms were removed respectively from the surface. The oxygen vacancy formation was found to depend significantly on the local structure and composition of the surface. The surface oxygen vacancy formation trends across the various surface terminations were found to hold for all the materials, irrespective of the 'B' site composition. The oxygen vacancy trends on the different (100) and (110) surface terminations for $La_{0.5}Sr_{0.5}CoO_3$ and $La_{0.5}Sr_{0.5}FeO_3$ are reported in Figure 9a and 9b, respectively, whereas the rest can be found in the supplementary information Figure S54(a-d). The surface oxygen vacancy formation energies were different from the average bulk oxygen vacancy formation energy. The energy to create $\delta = 0.125$ extent of oxygen vacancy in the bulk $La_{0.5}Sr_{0.5}CoO_3$ material was 0.275 eV/unit of ABO_3, while that on the 'AO' terminated (100) surfaces were much higher (in the ranges of $0.40\text{-}0.45$ ev/ABO_3). The oxygen vacancy formation energies on the 'BO' terminated surfaces were less than the bulk values. Co_SrO surface, in particular, was found to be really prone to accommodate the oxygen vacancies (vacancy formation energies found 0.125 eV lower than that of bulk). The (110) surfaces proved favorable towards oxygen vacancy generation as well. The oxygen-rich 'O'-terminations along (110) were the most favorable terminations for surface oxygen vacancy formation.

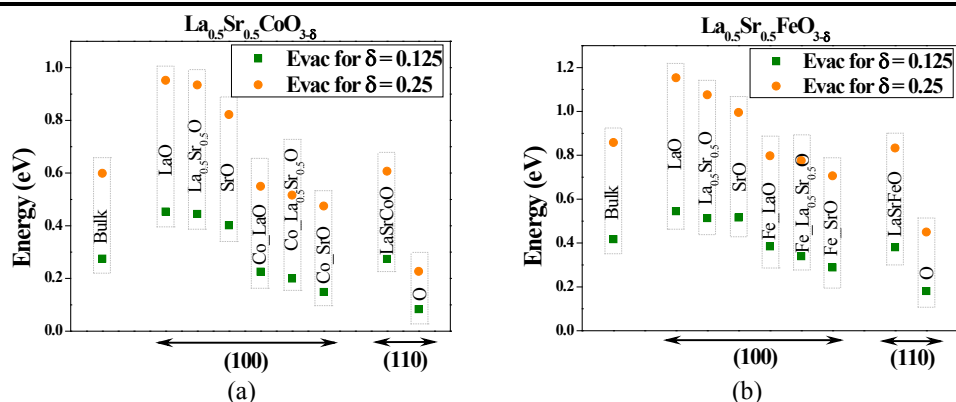*Corresponding author email: bhethana@usf.edu

Figure 9. Surface oxygen vacancy formation energy over various terminations along (100) and

(110) for (a) $La_{0.5}Sr_{0.5}CoO_{(3-\delta)}$ and (b) $La_{0.5}Sr_{0.5}FeO_{(3-\delta)}$

The same pattern was exhibited at higher concentrations of oxygen vacancy (δ = 0.25) as well. For $La_{0.5}Sr_{0.5}FeO_3$ (Figure 9b), and the other $La_{(1-x)}Sr_xFe_{(1-y)}Co_yO_3$ materials, as in Figure S54(a-d), the different surface terminations along (100) and (110) planes revealed a similar trend. Comparison among the oxygen vacancy formation energies in the bulk and across the 'AO' and 'BO' surface terminations for a vacancy extent of 0.125 is shown in Figure 10. This trend of oxygen vacancy formation across various surface terminations was found to be valid for all the six materials. This provides a basis for surface selection for optimum oxygen vacancy formation. Site specificity of these vacancy formation was also revealed. Figure 11(a-b) show the dependence of vacancy formation energy on the specific locations of AO terminated (100) surfaces. Oxygen vacancies along a linear chain was found favorable over a distributed vacancy formation (Figure 11a). For a higher extent of oxygen vacancy formation (δ = 0.25), a combination of sub-surface oxygen and surface oxygen removal was preferred over oxygen removal only from the top surface (Figure 11b).

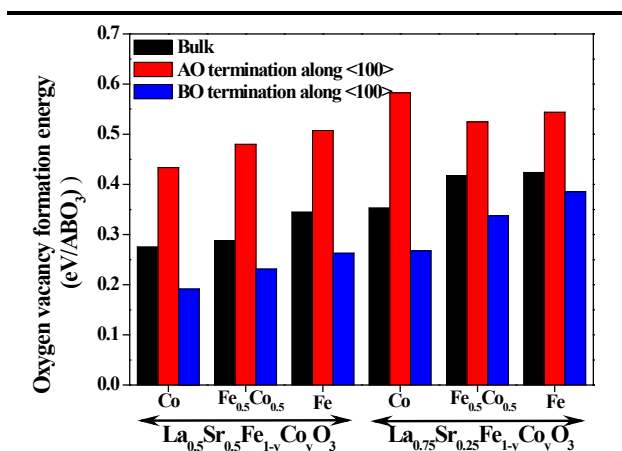*Corresponding author email: bhethana@usf.edu

Figure 10: Surface oxygen vacancy formation along 'AO' and 'BO' terminations of (100) planes
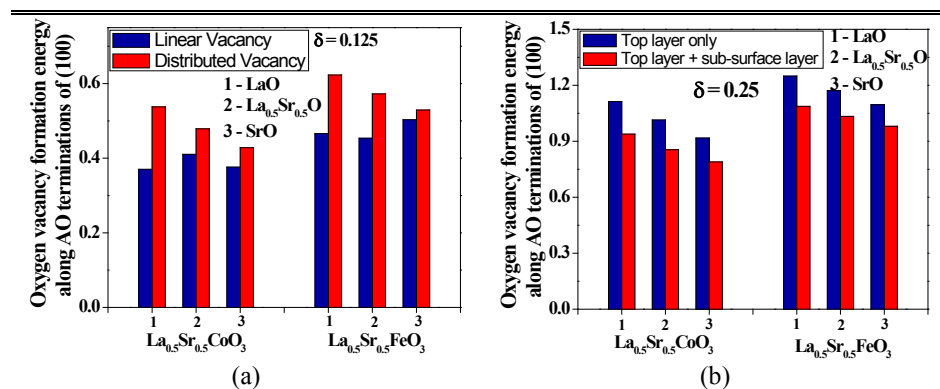
of $La_{(1-x)}Sr_xFe_{(1-y)}Co_yO_3$ [δ = 0.125]

Figure 11. Oxygen vacancy formation energies on different sites of AO surface terminations of

$La_{0.5}Sr_{0.5}BO_3$ (a) linear and distributed vacancy sites for (δ=0.125) and (b) oxygen vacancy

generation only on top surface and removal from both top and sub-surface.

The surface oxygen vacancy creation also results in significant amount of surface

reconstruction, often exchanging oxygen between two consecutive layers. Certain surface

terminations, particularly the 'BO' terminated surfaces [Figure S$\frac{5}{7}$(a)] were found to create

*Corresponding author email: bhethana@usf.edu

trench like regimes on the surface after losing the surface oxygen. These crevices can serve as potential active sites for gas phase reactions (CO_2 reduction for thermochemical cycles).

4.5. CO_2 adsorption studies:

The carbon dioxide adsorption energies on the perovskite surfaces are selected as descriptors for the CO_2 conversion reactions. The hypothesis is, stronger the adsorption, higher the tendency of carbon dioxide reduction to carbon monoxide. Use of oxygen and hydrogen adsorption energies as suitable descriptors had been done in past.[33, 34] Several studies on carbon dioxide adsorption on ceria and on metal surfaces have probed the best carbon dioxide adsorption configuration and the surface sites.[67, 68] The study here, comprised of only one of the adsorption states of carbon dioxide that has been compared over the different surface terminations of $La_{0.5}Sr_{0.5}FeO_3$ to reveal the role of oxygen vacancies and surface composition towards carbon dioxide conversion reactions. Although, the trends of adsorption energies over the various surface terminations and vacancy concentration are assumed to hold for different adsorption configurations, studying the explicit effects of the CO_2 adsorption configurations on CO_2 adsorption strengths across different surface terminations is in progress. CO_2 conversion experiments revealed a strong dependence on oxygen vacancies as in Figure 12 and computationally it has been done by Daza et al recently,[13] thus establishing that oxygen vacancy is the driving force for CO_2 thermo-chemical conversion process.

Comment [KJ2]: Word missing , reads like a fragment
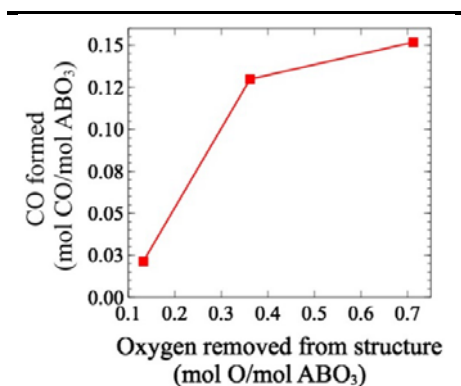
*Corresponding author email: bhethana@usf.edu

Figure 12: CO formation as a function of oxygen removed from ~~the surface~~ the $La_{0.5}Sr_{0.5}FeO_3$ surface during isothermal H_2-reduction in the RWGS-CL process at 550 °C.

Table 4. CO_2 adsorption strengths across stoichiometric and oxygen vacant surface terminations of $La_{0.5}Sr_{0.5}FeO_3$

Surface oxygen vacancy extent	CO_2 adsorption energies on various surface terminations of $La_{0.5}Sr_{0.5}FeO_3$ (eV)			
	La_O termination	Sr_O termination	Fe_LaO termination	Fe_SrO termination
$\delta=0$ [no vacancy]	-1.5135	-1.4822	-0.5736	-0.7800
$\delta=0.125$	-3.8411	-1.9044	-0.7458	-1.1189

The role of surface terminations was evident from Table 4; CO_2 adsorption strengths vary significantly across the different pure and non-stoichiometric surface terminations of $La_{0.5}Sr_{0.5}FeO_3$. The adsorption strengths increase on oxygen vacant surfaces which is in accord with the experimental results that state CO production rates increase with higher oxygen vacant surfaces as shown in Figure 12. CO_2 was found to bind stronger on the 'AO' surface terminations in comparison to the 'BO' terminations. The adsorption strength was highest on the oxygen vacant La_O termination thus making it quite promising for CO_2 conversion to CO.

*Corresponding author email: bhethana@usf.edu

5. Summary and conclusions:

A detailed investigation has been carried out on $La_{(1-x)}Sr_xFe_{(1-y)}Co_yO_{(3-\delta)}$ perovskite oxides. Computational studies via density functional theory has led to the proposition of probable crystal structure of the bulk materials. Increase of lattice constants for the cubic structures was noticed for increased iron content in the 'B' site. The various surface terminations along (100) and (110) crystal facets of these materials were tested for stability; revealing a consistent trend of higher stability of strontium-rich AO-terminated surface. This was true irrespective of the 'B' site composition. For the (110) surface terminations, the oxygen rich 'O' terminated planes was the natural choice for stability. The oxygen vacancy formation energetics both for the bulk systems and surface provided valuable insights. The trends of bulk oxygen vacancy formation energy were found to be in accord with the experimental results, whereby increasing iron content on the 'B' site led to higher energy cost for oxygen removal, while the reverse pattern was true for increasing strontium content on the 'A' site. There was a consistent trend of easy bulk oxygen vacancy formation from the lanthanum-layers while it was more energy intensive from strontium-rich layers, mainly due to the easier redistribution for electronic cloud in the lanthanum-layers. Localized or tunnel-like oxygen vacancy formation was also found favorable in comparison to a more distributed vacancy generation. The stability of these materials at high oxygen vacancy concentration were revealed computationally and through in-situ x-ray diffraction study of $La_{0.75}Sr_{0.25}CoO_3$ sample; thus making these materials a strong candidate for thermochemical reactions. On the other hand, the surface oxygen vacancy formation energy imparted valuable insights into the surface termination dependent oxygen vacancy generation. The 'BO' terminated (100) surfaces and (110) surfaces were favorable towards oxygen vacancy formation, while 'AO' terminated (100) planes proved reluctant towards the same. There was

*Corresponding author email: bhethana@usf.edu

also a strong dependence of surface oxygen vacancy formation energy on the various sites of surface terminations. The materials with different terminations were subsequently tested for carbon dioxide adsorption strengths as a descriptor for carbon dioxide conversion. Oxygen vacant 'AO' terminations along (100) surface proved to be strong candidates for possible CO_2 conversion sites. In the perspective of recent progress in preferential growth of surfaces of perovskites, this study paves the way towards determining the desired surfaces for the energy intensive CO_2 conversion reactions.

Associated Content:

Supplementary Information:

Bulk phase $La_{0.5}Sr_{0.5}FeO_3$ configurations; charge density plots for site specific oxygen vacancy formation; surface terminations along (110) crystal facets of $La_{(1-x)}Sr_xFeO_3$; surface oxygen vacancies of $La_{(1-x)}Sr_xFe_{(1-y)}Co_yO_3$; surface relaxations during oxygen vacancy formation

Author Information:

Notes

The authors declare no competing financial interest.

*Corresponding author email: bhethana@usf.edu

References:

1. G. Centi and S. Perathoner, *Catalysis Today*, 2009, **148**, 191-205.
2. G. Centi, E. A. Quadrelli and S. Perathoner, *Energy & Environmental Science*, 2013, **6**, 1711-1731.
3. D. Cheng, F. R. Negreiros, E. Aprà and A. Fortunelli, *ChemSusChem*, 2013, **6**, 944-965.
4. A. Steinfeld and R. Palumbo, *Journal*, 2001, **15**, 237-256.
5. T. Kodama and N. Gokon, *Chem. Rev.*, 2007, **107**, 4048-4077.
6. W. C. Chueh, C. Falter, M. Abbott, D. Scipio, P. Furler, S. M. Haile and A. Steinfeld, *Science*, 2010, **330**, 1797-1801.
7. J. R. Scheffe and A. Steinfeld, *Energy & Fuels*, 2012, **26**, 1928-1936.
8. P. Furler, J. R. Scheffe, M. Gorbar, L. Moes, U. Vogt and A. Steinfeld, *Energy & Fuels*, 2012, **26**, 7051-7059.
9. A. H. McDaniel, E. C. Miller, D. Arifin, A. Ambrosini, E. N. Coker, R. O'Hayre, W. C. Chueh and J. Tong, *Energy & Environmental Science*, 2013, **6**, 2024-2028.
10. D. S. Mallapragada, N. R. Singh, V. Curteanu and R. Agrawal, *Industrial & Engineering Chemistry Research*, 2013, **52**, 5136-5144.
11. J. R. Scheffe, D. Weibel and A. Steinfeld, *Energy & Fuels*, 2013, **27**, 4250-4257.
12. Y. A. Daza, R. A. Kent, M. M. Yung and J. N. Kuhn, *Industrial & Engineering Chemistry Research*, 2014, **53**, 5828-5837.
13. Y. A. Daza, D. Maiti, R. A. Kent, V. R. Bhethanabotla and J. N. Kuhn, *Catalysis Today*, 2015, **258, 2**, 691-698.
14. Q. Jiang, J. Tong, G. Zhou, Z. Jiang, Z. Li and C. Li, *Solar Energy*, 2014, **103**, 425-437.
15. M. A. Peña and J. L. G. Fierro, *Chemical Reviews*, 2001, **101**, 1981-2017.
16. D. Klvana, J. Kirchnerová and C. Tofan, *Korean J. Chem. Eng.*, 1999, **16**, 470-4777.
17. M. Godickemeier, K. Sasaki, L. J. Gaukler and I. Reiss, *Solid State Ionics*, 1996, **86-88, 2**, 691-701.
18. T. Ishihara, in *Perovskite Oxide for Solid Oxide Fuel Cells*, ed. T. Ishihara, Springer US, 2009, DOI: 10.1007/978-0-387-77708-5_1, ch. 1, pp. 1-16.
19. J. Mizusaki, H. Tagawa, K. Naraya and T. Sasamoto, *Solid State Ionics*, 1991, **49**, 111-118.
20. A. Mineshige, J. Abe, M. Kobune, Y. Uchimoto and T. Yazawa, *Solid State Ionics*, 2006, **177**, 1803-1806.
21. A. H. Bork, M. Kubicek, M. Struzik and J. L. M. Rupp, *Journal of Materials Chemistry A*, 2015, **3**, 15546-15557.

*Corresponding author email: bhethana@usf.edu

22. A. M. Deml, V. Stevanović, C. L. Muhich, C. B. Musgrave and R. O'Hayre, *Energy & Environmental Science*, 2014, **7**, 1996-2004.

23. A. M. Deml, V. Stevanović, A. M. Holder, M. Sanders, R. O'Hayre and C. B. Musgrave, *Chemistry of Materials*, 2014, **26**, 6595-6602.

24. M. T. Curnan and J. R. Kitchin, *Journal of Physical Chemistry C*, 2014, **118**, 28776−28790.

25. X. Ma, B. Wang, E. Xhafa, K. Sun and E. Nikolla, *Chem Commun (Camb)*, 2015, **51**, 137-140.

26. X. Ma, J. S. A. Carneiro, X.-K. Gu, H. Qin, H. Xin, K. Sun and E. Nikolla, *ACS Catalysis*, 2015, **5**, 4013-4019.

27. C. Hou, W. Feng, L. Yuan, K. Huang and S. Feng, *CrystEngComm*, 2014, **16**, 2874-2877.

28. F. Sanchez, C. Ocal and J. Fontcuberta, *Chem Soc Rev*, 2014, **43**, 2272-2285.

29. U. Treske, N. Heming, M. Knupfer, B. Büchner, A. Koitzsch, E. Di Gennaro, U. Scotti di Uccio, F. Miletto Granozio and S. Krause, *APL Materials*, 2014, **2**, 012108-012101 - 012108-012108.

30. Y. Orikasa, E. J. Crumlin, S. Sako, K. Amezawa, T. Uruga, M. D. Biegalski, H. M. Christen, Y. Uchimoto and Y. Shao-Horn, *ECS Electrochemistry Letters*, 2014, **3**, F23-F26.

31. Z. Feng, Y. Yacoby, M. J. Gadre, Y. L. Lee, W. T. Hong, H. Zhou, M. D. Biegalski, H. M. Christen, S. B. Adler, D. Morgan and Y. Shao-Horn, *J Phys Chem Lett*, 2014, **5**, 1027-1034.

32. J. Druce, H. Tellez, M. Burriel, M. D. Sharp, L. J. Fawcett, S. N. Cook, D. S. McPhail, T. Ishihara, H. H. Brongersma and J. A. Kilner, *Energy & Environmental Science*, 2014, **7**, 3593-3599.

33. J. L. C. Fajín, M. N. D. S. Cordeiro, F. Illas and J. R. B. Gomes, *Journal of Catalysis*, 2010, **276**, 92-100.

34. J. L. C. Fajín, M. N. D. S. Cordeiro, F. Illas and J. R. B. Gomes, *Journal of Catalysis*, 2014, **313**, 24-33.

35. J. K. Norskov, T. Bligaard, J. Rossmeisl and C. H. Christensen, *Nature Chemistry*, 2009, **1**, 37-46.

36. P. Hohenberg and W. Kohn, *Physical Review*, 1964, **136**, B864-B871.

37. W. Kohn and L. J. Sham, *Physical Review*, 1965, **140**, A1133-A1138.

38. G. Kresse and J. Furthmüller, *Computational Materials Science*, 1996, **6**, 15-50.

39. G. Kresse and J. Hafner, *Physical Review B*, 1993, **47**, 558-561.

40. G. Kresse and J. Furthmüller, *Physical Review B*, 1996, **54**, 11169-11186.

41. P. E. Blöchl, *Physical Review B*, 1994, **50**, 17953-17979.

42. G. Kresse and D. Joubert, *Physical Review B*, 1999, **59**, 1758-1775.

43. J. P. Perdew and Y. Wang, *Physical Review B*, 1992, **45**, 13244-13249.

44. L. Bengtsson, *Physical Review B*, 1999, **59**, 12301-12304.

*Corresponding author email: bhethana@usf.edu

45. L. Wang, T. Maxisch and G. Ceder, *Physical Review B*, 2006, **73**, 195107-195101 - 195107-195106.

46. Y.-L. Lee, J. Kleis, J. Rossmeisl and D. Morgan, *Physical Review B*, 2009, **80**, 224101-224101 - 224101-224120.

47. G. Henkelman, A. Arnaldsson and H. Jónsson, *Computational Materials Science*, 2006, **36**, 354-360.

48. E. Sanville, S. D. Kenny, R. Smith and G. Henkelman, *Journal of Computational Chemistry*, 2007, **28**, 899-908.

49. W. Tang, E. Sanville and G. Henkelman, *J Phys Condens Matter*, 2009, **21**, 084204-084201 - 084204-084207.

50. K. Momma and F. Izumi, *Journal of Applied Crystallography*, 2011, **44**, 1272-1276.

51. Y. A. Daza, D. Maiti, B. J. Hare, V. R. Bhethanabotla and J. N. Kuhn, *Surface Science*, 2015, doi:10.1016/j.susc.2015.11.017, In press.

52. A. T. R. Simon, *Journal of Physics: Condensed Matter*, 1996, **8**, 8267-8275.

53. S. Švarcová, K. Wiik, J. Tolchard, H. J. M. Bouwmeester and T. Grande, *Solid State Ionics*, 2008, **178**, 1787-1791.

54. B. P. Uberuaga and G. Pilania, *Chemistry of Materials*, 2015, **27**, 5020-5026.

55. T. L. Nguyen, M. Dokiya, S. Wang, H. Tagawa and T. Hashimoto, *Solid State Ionics*, 2000, **130**, 229-241.

56. I. Kagomiya, K. Jimbo, K.-i. Kakimoto, M. Nakayama and O. Masson, *Physical Chemistry Chemical Physics*, 2014, **16**, 10875-10882.

57. C. N. R. a. G. Rao, J., *New Directions in Solid State Chemistry*, Cambridge University Press, 1986.

58. T. R. S. Prasanna and A. Navrotsky, *Journal of Materials Research*, 1993, **8**, 1484-1486.

59. Y.-M. Kim, J. He, M. D. Biegalski, H. Ambaye, V. Lauter, H. M. Christen, S. T. Pantelides, S. J. Pennycook, S. V. Kalinin and A. Y. Borisevich, *Nat Mater*, 2012, **11**, 888-894.

60. J. N. Kuhn and U. S. Ozkan, *Journal of Catalysis*, 2008, **253**, 200-211.

61. T. X. T. Sayle, S. C. Parker and C. R. A. Catlow, *Surface Science*, 1994, **316**, 329-336.

62. G. Lu, A. Linsebigler and J. T. Yates, *The Journal of Physical Chemistry*, 1995, **99**, 7626-7631.

63. M. A. Henderson, W. S. Epling, C. L. Perkins, C. H. F. Peden and U. Diebold, *The Journal of Physical Chemistry B*, 1999, **103**, 5328-5337.

64. C. T. Campbell and C. H. F. Peden, *Science*, 2005, **309**, 713-714.

*Corresponding author email: bhethana@usf.edu

65. C. Yang, L.-L. Yin, F. Bebensee, M. Buchholz, H. Sezen, S. Heissler, J. Chen, A. Nefedov, H. Idriss, X.-Q. Gong and C. Wöll, *Physical chemistry chemical physics : PCCP*, 2014, **16**, 24165-24168.

66. R. Schaub, P. Thostrup, N. Lopez, E. Lægsgaard, I. Stensgaard, J. K. Nørskov and F. Besenbacher, *Physical Review Letters*, 2001, **87**, 266104-266101 - 266104-266104

67. Z. Cheng, B. J. Sherman and C. S. Lo, *The Journal of Chemical Physics*, 2013, **138**, 014702: 014701-014712.

68. P. M. Albrecht, D.-e. Jiang and D. R. Mullins, *The Journal of Physical Chemistry C*, 2014, **118**, 9042-9050.

*Corresponding author email: bhethana@usf.edu